

# ROTORCRAFT FLIGHT IN INTERACTION WITH OBSTACLES

Theologos E. Andronikos, Dimitirs I. Manolas, Vasilis A. Riziotis, Spyros G. Voutsinas  
National Technical University of Athens, NTUA, 9 Heron Polytechniou str., 15780 Athens Greece

## ABSTRACT

Helicopter flight in time and spatially varying inflow environments sets special requirements for its design and it is closely linked to its utilization and operation envelope (classification). Commonly, definition of the abovementioned non-conventional inflow conditions in the standards relies on evidence coming from pilots' reports while theoretical or experimental studies usually follow either to confirm or to revise or to update provisions of the standards. Such a non conventional flight scenario, which is the focus of the present paper, is when a helicopter performs hover flight in proximity to obstacles. Helicopters are largely employed in missions within confined areas, regions in which the flight of the helicopter is limited in some direction by the terrain or by the presence of obstacles. During approaching or landing under the above described circumstances an unsteady flow field is developed in the region between the rotor and the obstacle that has not been studied in detail. Moreover, interaction between the rotor and the obstacle is not yet well understood especially in cases that obstacles generate wakes. As a result of this interaction unsteady aerodynamic loads are developed over the obstacles and flight characteristics and controllability of the rotor might be affected.

Keywords: Rotor aerodynamics, interaction with obstacles, wake interactions

## 1 INTRODUCTION

Flight in confined areas or in proximity to natural or manmade obstacles is commonly part of helicopters' operational envelope. Frequently civil helicopters fly in proximity to building blocks when for example performing rescue flights within residential areas<sup>1</sup>, while military helicopters land on ships of irregular shapes<sup>2</sup>. The above are only two characteristic examples of flight in interaction with obstacles. During flight under the above mentioned conditions, interaction of the rotor wake with the obstacle takes place affecting the loading of the rotor. Moreover, an unsteady aerodynamic field is developed in the region between the rotor and the obstacle that induces time varying pressures on the obstacles. These interactional phenomena as well as the parameters of the problem that are important for the design of helicopters have not been studied in detail by the helicopter community. Recognition of the importance of such interactions as well as of the existing knowledge gap hassled GARTEUR to the formation of a specific action group on this topic (AG-22)<sup>3</sup>.

The aim of the present paper is to numerically study the above mentioned aerodynamic interactional phenomena in an integrated framework that also considers aeroelastic coupling. For the aerodynamic modeling of the helicopter rotor the in-house GenUVP<sup>4</sup> code is employed. GenUVP is a potential flow solver combining a panel representation of the blades with a free vortex particles representation of the wake. A particle mesh approach based on the

solution of Poisson equation for vector potential is applied in the calculation of the wake convection velocities<sup>5</sup>. For the structural modeling of the rotor the in-house code hGAST<sup>6</sup> is used. A multi-body representation of the flexible blades is employed in hGAST. The problem of the aerodynamic interaction of the rotor with the obstacle is treated in a fully coupled manner through a panel representation of the obstacles with the option of emitting vorticity from their edges. In this way the wake generated by the obstacles is simulated. The presence of the ground is considered through symmetry condition (mirroring approach).

For the analysis of the problem three case studies are considered. The first case study concerns the aerodynamic characteristics of a helicopter in hover flight above a rectangular obstacle for which wind tunnel measurements have been performed by Polytechnic di Milano (POLIMI)<sup>7</sup>. In this case the development of the interactive flow is studied in terms of the averaged flow field that is established together with the aerodynamic loads on the rotor. Predictions are compared to measurements. The aim of this part is to check the validity of inviscid simulations for different proximity conditions as defined by the relative position of the helicopter in the horizontal and/or vertical direction. Thrust and flow-field patterns close to the obstacles are used as indicators.

The second case study concerns hover flight of a helicopter within a squared shaped court-yard for which measurements have been performed by ONERA<sup>3</sup>. Simulations of the hover flight at different

heights from the ground and in varying distances with and without the presence of side walls are performed. The pressure distributions on the ground/buildings, as well as the rotor thrust are compared to experimental data. In this part, the aim is to validate the flow solver in ground effect and its ability to analyse the flow field established within the confined area of the court-yard.

Finally aeroelastic analysis of a scaled BO105 rotor (scale factor 2.5) is performed in proximity to an obstacle. Rotor load results are presented for the rotor interacting with the obstacle.

## 2 FORMULATION OF THE METHOD

### 2.1 The flow solver

In the modelling of the flow GenUVP code combines a panel method<sup>8</sup> with a vortex particle representation of the wake<sup>9,4,10</sup>. The theoretical backbone of the method is Helmholtz's decomposition theorem<sup>11</sup> according to which any flow-field  $\vec{u}$  can be decomposed into a potential part  $\vec{u}_{solid} = \nabla\phi$  associated with the presence of the solid boundaries (blades and/or obstacles) in the flow and a vortical part  $\vec{u}_{wake} = \nabla \times \vec{\psi}$  associated with the wake or the free vorticity  $\vec{\omega}$  where  $\phi$  and  $\vec{\psi}$  denote the scalar and the vector potentials of the flow respectively satisfying field equations:

$$(1) \quad \nabla^2 \phi = \nabla \cdot \vec{u} \equiv \Delta$$

and

$$(2) \quad \nabla^2 \vec{\psi} = -\nabla \times \vec{u} \equiv -\vec{\omega}$$

Then Green's theorem provides integral representations for both parts which in the case of an inviscid and incompressible flow take the following form:

$$(3) \quad \begin{aligned} \vec{u}_{solid}(\vec{x};t) &= \int_{S(t)} \frac{(\sigma \cdot + \vec{\gamma} \times) \vec{r}}{4\pi \vec{r}^3} dS(\vec{y}) \\ \vec{u}_{wake}(\vec{x};t) &= \int_{D_\omega(t)} \frac{\vec{\omega}(\vec{y};t) \times \vec{r}}{4\pi \vec{r}^3} dD(\vec{y}) \end{aligned}$$

In (3)  $\vec{r} = \vec{x} - \vec{y}$ ,  $D_\omega(t)$  denotes the region covered by the wake,  $S(t)$  denotes collectively the solid boundaries and  $\sigma, \vec{\gamma}$  denote the surface source and vorticity distributions associated with the normal and tangent to  $S$  velocity components. By construction they both vanish at infinity so the velocity at infinity  $\vec{u}_{ext}$  must be added in order to form  $\vec{u}$ .

Based on the above kinematic formulation, the flow equations to be satisfied are:

- The no-penetration boundary condition:  $\vec{u} \cdot \vec{n} = \vec{U}_s \cdot \vec{n}$  where  $\vec{U}_s$  denotes the body velocity.  $\vec{U}_s$  will include the rotational speed, the speed induced by the pitch control as well as the deformation velocity of flexible blades.
- The vorticity emission condition also known as Kutta condition. It is applied on the solid surface at predefined lines such as the trailing edge or blade tips; wherefrom the bound vorticity is released continuously in the free flow so as to form the wake. It imposes zero pressure jump across the wake at the emission line.
- The Helmholtz equations, i.e. the momentum equations written with respect to vorticity.

In potential theory wakes are introduced as material surfaces carrying surface vorticity  $\vec{\gamma}$ . Existing wake models differ on the choice of elements to describe the wake but most importantly on whether they assume connectivity among these elements. Connectivity is necessary in order to satisfy the fundamental requirement that vorticity is div free or else that the vorticity lines in the wake are either closed or they start and end on a solid boundary or at infinity. These requirements are by construction fulfilled when the wake is formed by means of vortex filaments or is retained as a surface. Connectivity however can generate numerical problems when the wake is excessively deformed or interacts with solid bodies as in the present case. In order to bypass this problem, GenUVP uses freely moving vortex blobs. They are 3D point vortices equipped with core. Vortex blobs are generated at every time step in a two-steps procedure. First the wake is released in the form of surface vorticity. It is in this form that the no-penetration and Kutta conditions are satisfied. Then the convection step is carried out during which surface vorticity is integrated and transformed into vortex blobs defined by their intensities  $\vec{\Omega}_p$ , their positions  $\vec{Z}_p$  and their core sizes  $\varepsilon_p$ :

$$(4) \quad \vec{\omega}(\vec{x};t) \cong \sum_p \vec{\Omega}_p(t) \zeta_\varepsilon(\vec{x} - \vec{Z}_p(t))$$

where  $\zeta_\varepsilon$  is the cut-off or distribution function defined over the core. GenUVP uses a cubic exponential function<sup>12</sup> which results in the following velocity representation:

$$(5) \quad \vec{u}_{wake}(\vec{x};t) = \sum_p \frac{\vec{\Omega}_p(t) \times \vec{r}_p}{4\pi r^3} (1 - \exp(-r^3 / \varepsilon^3))$$

where  $\vec{r}_p = \vec{x} - \vec{Z}_p$ .

The integration satisfies the basic invariant properties of fluid flows:

$$(6) \quad \begin{aligned} \bar{\Omega}_p(t) &= \int_{D_p} \bar{\omega}(\bar{y};t) dD, \\ \bar{\Omega}_p(t) \times \bar{Z}_p(t) &= \int_{D_p} \bar{\omega}(\bar{y};t) \times \bar{y} dD \end{aligned}$$

while  $\bar{\Omega}_p$  and  $\bar{Z}_p$  are determined by integrating in time the corresponding evolution equations:

$$(7) \quad \frac{d\bar{Z}_p(t)}{dt} = \bar{u}(\bar{Z}_p;t), \quad \frac{d\bar{\Omega}_p(t)}{dt} = (\bar{\Omega}_p(t) \nabla) \bar{u}(\bar{Z}_p;t)$$

Being unconnected, vortex blobs will generate a vorticity field which will eventually violate in time the div free requirement. There are two methods to correct this error: (a) either by remeshing or (b) by using the Particle-Mesh method. Fortunately the Particle-Mesh method offers additionally a substantial reduction of computational cost and it has been implemented in GenUVP. The vorticity of the wake vortex particles is first projected on a Cartesian grid and then the Poisson equation  $\nabla^2 \bar{\psi} = -\bar{\omega}$  is solved over the same grid by means of a fast Fourier transformation solver<sup>5</sup>. Then  $\bar{u}_{wake} = \nabla \times \bar{\psi}$  and its derivatives appearing in (7) are calculated through finite differences.

## 2.2 The elastic model

Nonlinear time domain aeroelastic simulations are performed using NTUA's in-house aero-elastic solver hGAST<sup>6</sup>. In hGAST, the helicopter is considered as a multi-component dynamic system where all flexible components/bodies are approximated as Timoshenko beam structures (e.g. main rotor blades and shaft, tail rotor blades). Assembly of the above components into the full system is carried out in the framework of the so called multibody approach. It consists of considering each component separately from the others but subjected to specific free-body kinematic and loading conditions that are imposed at the connection points of the components.

In the multibody context, a local coordinate system is assigned to each component/body with respect to which local elastic displacements are defined. The local frame of each body is subjected to rigid body and elastic motions communicated by preceding bodies as kinematic conditions imposed at their connection points. Rigid body motions can be either prescribed or controlled while elastic motions consist of the total deflection of the previous components "transferred" to the current component. For example, the blades are subjected to elastic translational and rotational motions of the drive train as well as to rigid body motions as the pitching motion or the teetering motion in case of two bladed rotor (directly imposed on the blades) or azimuthal rotation (indirectly

imposed on the blades through the drive train). In addition to the kinematic conditions imposed on the connection points, loading conditions must be also satisfied. In particular, at each connection point, one of the connected bodies contributes the displacements and rotations to all others, which in turn contribute their internal (reaction) loads.

The same multibody formulation is also extendable to the component level which is actually implemented in hGAST. Highly flexible components, such as the blades, are divided into a number of interconnected sub-bodies, each considered as a single linear beam element or as an assembly of linear beam elements. Large deflections and rotations are gradually built and nonlinear dynamics are introduced by imposing to each sub-body, the deflections and rotations of preceding sub-bodies as rigid body motions. Dynamic coupling of the sub-bodies is introduced by communicating the reaction loads (3 forces and 3 moments) at the first node of each sub-body to the free node of the previous sub-body as external load.

## 3 RESULTS

In the following sections, comparisons of model predictions against measured data from the databases of POLIMI<sup>7</sup>, and ONERA<sup>3</sup>, are presented. The above comparisons concern pure aerodynamic data (i.e. aerodynamic loads on the rotor and pressure distributions over the obstacles). In addition to the above comparisons, aeroelastic simulations of a BO105 model (scale down factor of 2.5) flying in proximity to an obstacle are analyzed and assessment of the vibrations of the main rotor is performed.

### 3.1 Comparison against POLIMI database

POLIMI conducted a measurement campaign for a helicopter with a four bladed main rotor in proximity to a well shaped rectangular obstacle. Two different cases were examined:

Case 1: Hover flight in ground effect (IGE) in large distance from the obstacle

Case 2: Hover flight above/near the obstacle

#### 3.1.1 Experimental setup

The main rotor of the helicopter has a diameter of 0.75 m and a constant chord of 0.032 m. The blades are formed by NACA 0012 airfoils. The pitch angle is fixed at 10° (nose up) and the rotor speed is set at a nominal value of 2580 RPM. Small variations of +/- 2% with respect to this nominal value were recorded during the tests. The obstacle is a rectangular box with dimensions 1 m in the x-axis (wind direction), 0.8 m in the y-axis and 0.4 m in z-axis (height), as shown in Figure 1.

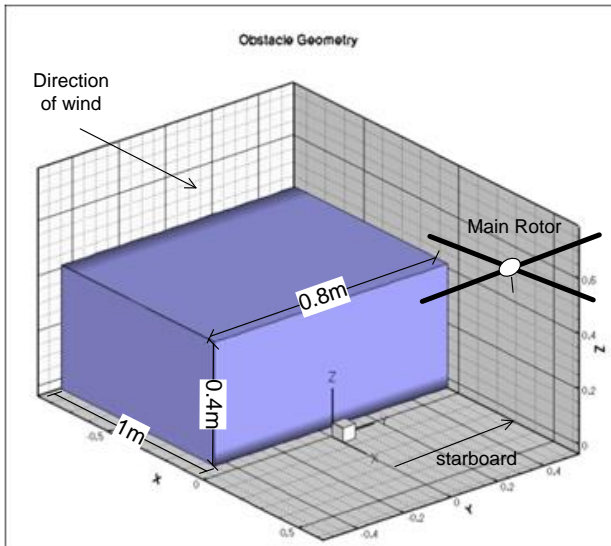


Figure 1 Global View of Obstacle/Rotor layout.

The database includes one IGE test case and 4 test cases with obstacle interaction. All test cases have been conducted at advance ratios of  $\mu = 0.0$  and  $0.05$ .

Table 1 presents the matrix of tests conducted by POLIMI. The cases marked in bold have been selected for the present analysis. The first corresponds to hover only in ground effect while the other two also include the obstacle. In Case T1 the helicopter rotor is centered with respect to the obstacle and a position sweep in the vertical direction is undergone. In Case T2 a horizontal sweep of the helicopter position is performed (see Figure 2).

### 3.1.2 Computational setup

Blades are represented as thin lifting surfaces carrying piecewise constant dipole distributions while the obstacle is approximated as a non lifting body represented by piecewise constant sources distribution. The fuselage of the helicopter is not considered in the simulations. No vorticity emission takes place from the edges of the obstacles. The presence of the ground is accounted for through symmetry condition (mirroring approach).

Test name	Obstacle	Sweep Direction	X/R	Y/R	Z/R	First Point	Last Point	Number of Points
IGE	NO	Z	0	0	-	Z/R=1	Z/R=4	10
T1	YES	Z	-1.07	0	-	Z/R=2	Z/R=4	7
T2	YES	X	-	0	2	X/R=-1	X/R=1	5
T3	YES	Z	2	0	-	Z/R=1	Z/R=4.2	9
T4	YES	Z	2	-1.33	-	Z/R=1	Z/R=4.2	9

Table 1. Campaign test matrix.

Preliminary simulations indicated that for an isolated rotor convergence to a periodic state is reached after 20 full revolutions. The results shown in the sequel correspond to azimuthally averaged load values after the 21<sup>st</sup> revolution and for 20 revolutions.

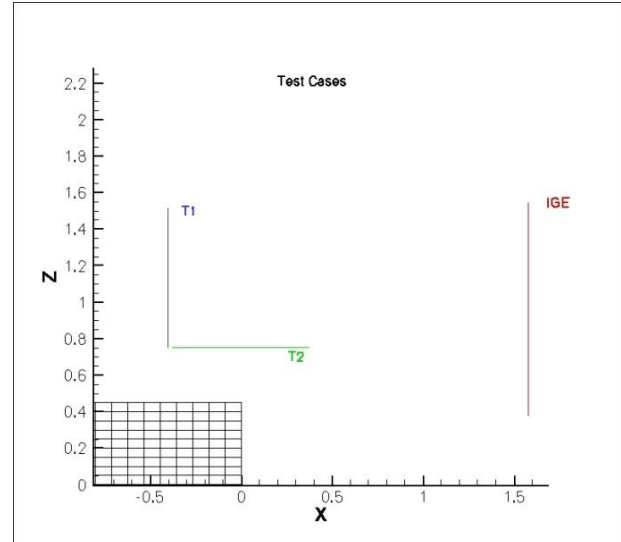


Figure 2. Sweeping direction in simulated test cases.

### 3.1.3 Rotor loads comparisons

In Figure 3 to Figure 8 the predicted thrust and torque of the main rotor are compared against measured data for test cases IGE, T1 and T2 of Table 1.

In the IGE case, the agreement in terms of shape and values is good over the complete range of heights considered (see Figure 3 and Figure 4). An increase of ~15% in thrust and 4% in torque with respect to the hover flight case without ground effect (IGE, Z/R=4) is noted as the helicopter distance from the ground decreases from 4R (1.5 m) to 1R (0.375 m). At 4R the effect of the ground becomes almost negligible. The maximum difference between predictions and measurements is ~3% in thrust and 1% in torque results. The variations of the thrust and torque do not follow the exponential behaviour derived from analytical considerations<sup>13</sup>. Instead, at z=0.65m a knee appears which is more pronounced in the torque results. The distance at which this change takes place is correctly predicted while the overshoot in torque is slightly overestimated. At this distance, the wake that bounces back after impinging on the ground lies within the rotor area and therefore affects the rotor.

Predicted and measured thrust and torque results for test case T1 (vertical sweep above the centre of the obstacle – see Figure 2) are presented in Figure 5 and Figure 6. The rotor thrust force in this case increases faster with height as a result of the

presence of the obstacle. Already at the distance of  $2R$  (0.75 m) from the ground the increase in thrust is 18% while the increase in torque is about 4%. In the thrust results, the difference between predictions and measurements increases as the helicopter moves closer to the obstacle (for heights less than  $1.5D$ ). In the torque results the maximum difference appears in the vicinity of 0.9 m height. The maximum difference between predictions and measurements is in the order of 5% in thrust and 2.5% in torque. It is worth noting that in the T1 case variation of thrust and torque in the measurements is much smoother than in the previous IGE case. On the contrary the predicted thrust and torque present a deep in between the heights of 0.9 to 1 m. This is again attributed to the back bouncing of the rotor wake as seen in the IGE case. In a potential flow solver, lack of viscous effects will render the evolution of this bouncing effect more pronounced. At the height of  $4R$  the rotor thrust and torque are almost equal to those of the IGE case at the same height indicating that the interaction at this height is rather weak.

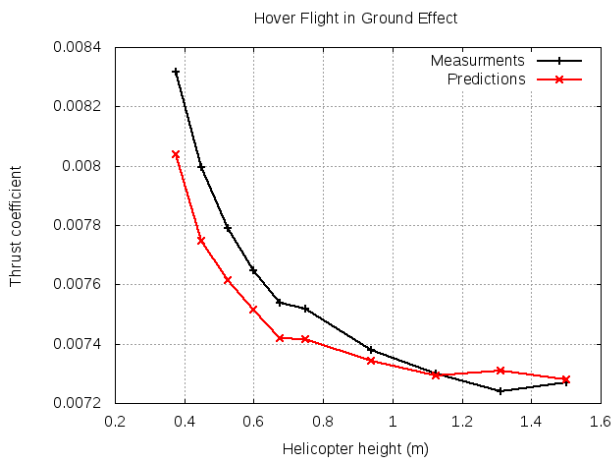


Figure 3. Test Case IGE. Variation of Thrust with height.

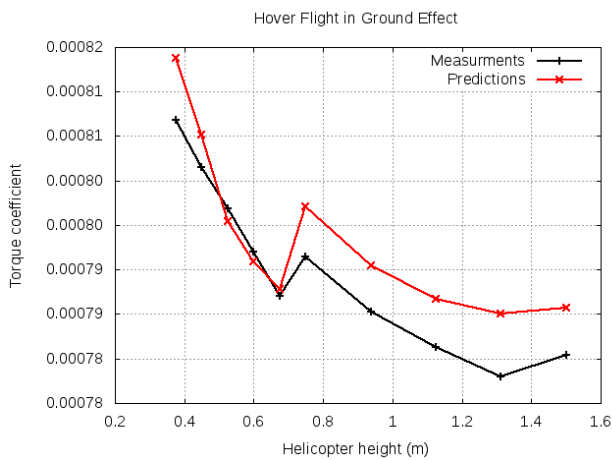


Figure 4. Test Case IGE. Variation of Torque with height.

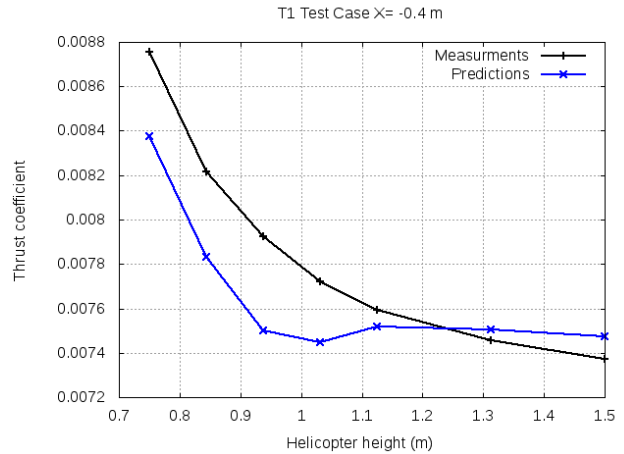


Figure 5. Test Case T1. Variation of Thrust with height.

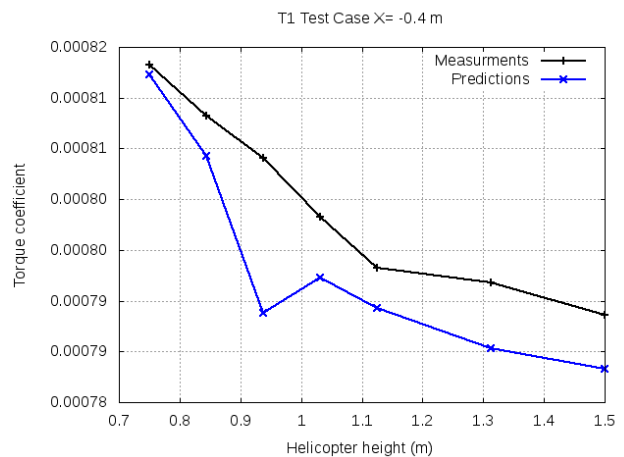


Figure 6. Test Case T1. Variation of Torque with height.

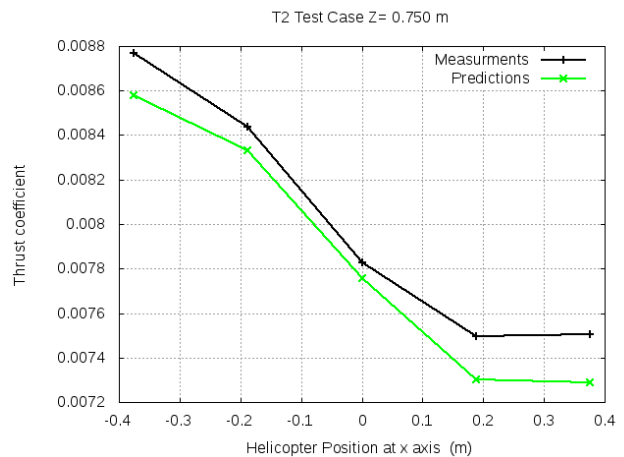


Figure 7. Test Case T2. Variation of Thrust with horizontal distance.

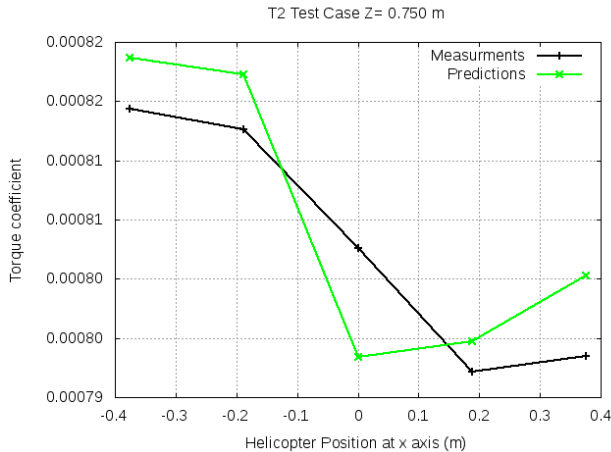


Figure 8. Test Case T2. Variation of Torque with horizontal distance.

In Case T2 a horizontal sweep of the helicopter position is considered keeping the vertical position at  $z=2R$  from the ground (0.35 m from the obstacle - Figure 2). The sweep starts considering the rotor centered with respect to the obstacle and ends at  $1R$  from the edge of the obstacle. As depicted in Figure 7 and Figure 8 maximum thrust and torque are obtained when the rotor is right above the centre of the obstacle (at  $x = -0.4 m$ ). As the rotor is displaced in the  $x$  direction, thrust and torque drop. In the tests minimum thrust and torque is measured at  $x = 0.2 m$  ( $\sim 0.5R$  from the edge of the obstacle). Beyond this point thrust remains almost constant while torque slightly increases. The variation in thrust is well predicted over the entire sweep. Torque predictions are less good: minimum torque is predicted sooner at  $x = 0 m$  and also the subsequent increase is higher. The maximum difference between predictions and measurements is  $\sim 3\%$  in thrust and  $1.5\%$  in torque.

### 3.1.4 Flow field comparisons

In the present section, the flow field characteristics are analysed through comparisons with PIV measurements. PIV data are available on  $xz$  planes placed at  $y=0$  (see coordinate system in Figure 1) for different  $x$  positions of the rotor with respect to the obstacle all corresponding to a vertical placement at  $z=1R$  from the ground. Time averaged velocities over a time period of 1 revolution are compared.

When the rotor is centred over the obstacle, flow measurements indicate (as shown in Figure 9) that the strong downwash flow induced by the rotor wake separates over the edges of the obstacle upper surface and a re-circulation zone of low velocities is formed which remains attached to the obstacle side face. High downwards wake velocities are obtained

at the edge of the re-circulation zone. So, as a result of the flow separation the wake of the rotor expands to a distance equal to the size of the separation bubble. In the predictions (see Figure 10), the absence of vorticity emission from the edges of the obstacle, which potentially could simulate flow separation, causes the streamlines to closely follow the shape of the obstacle. As a result, high downwash velocities are obtained over the side face of the obstacle. The vortices appearing at  $x=400 mm$  and  $750mm$  are related to the roll up of the wake that hits the ground. The above qualitative differences between the measured and predicted flow patterns may explain the higher differences obtained in the loads (see Figure 5) as the rotor approaches the obstacle.

When the rotor centre is aligned with the edge of the obstacle, a recirculation area is again created. The measured flow pattern in Figure 11 is similar to the one shown in Figure 9 and only differs in the intensity of the downwash stream passing over the edge of the obstacle. In the predicted flow field (Figure 12) the downstream is equally strong but displaced in  $x$  direction forming an area of low velocity on its left and up to the obstacle. The strong slipstream may be identified to the tip vortices that are seen on the right part of the downwash in Figure 12. The left part of the measured downwash may be identified to the combined effect of the fuselage and the separation along the edge of the obstacle. The fact that none of these two effects is included in the simulations may explain the formation of the low speed area predicted in between the downwash and the obstacle. Further to that, in the simulation, two distinct vortex structures of counter direction are formed. These structures are related to the impingement process of the rotor wake which splits in two parts. The one on the left is trapped into the down corner of the obstacle while the one on the right develops into a weak roll-up.

When the rotor centre is moved at  $x/R= 0.5$ , the re-circulation zone disappears (Figure 13). This is because in this case the rotor downwash flow is almost parallel to the side face of the obstacle. Two counter rotating vortices are formed within the measured window; the one corresponds to the roll up of the wake of the retreating side near the ground level and the second corresponds to the interaction of the wake of the retreating side with the wake of the advancing sides. In this case the predicted flow pattern (Figure 14) agrees quite well with the measured one. The two vortices are well captured. The only difference is that in the simulations the lower vortex is pushed closer to the ground.

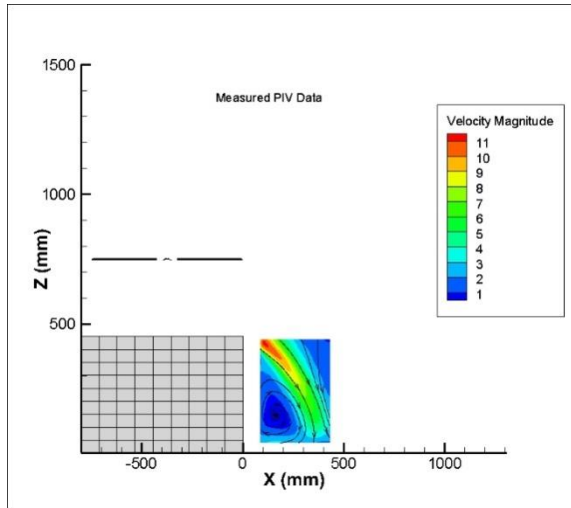


Figure 9. Measured flow pattern characteristics (averaged velocities). Rotor centre located at  $x/R = -1$ .

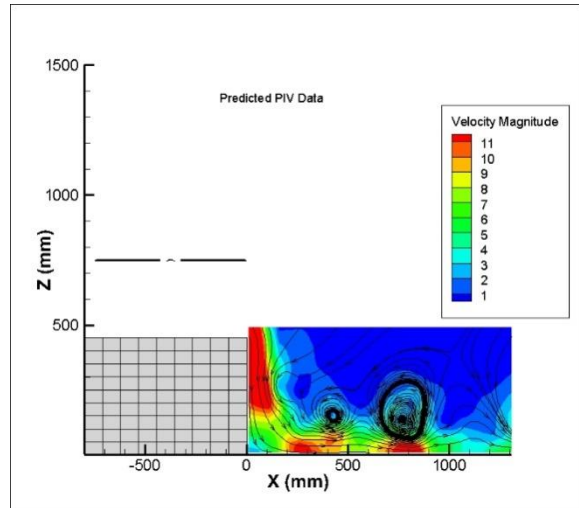


Figure 10. Predicted flow pattern characteristics (averaged velocities). Rotor centre located at  $x/R = -1$ .

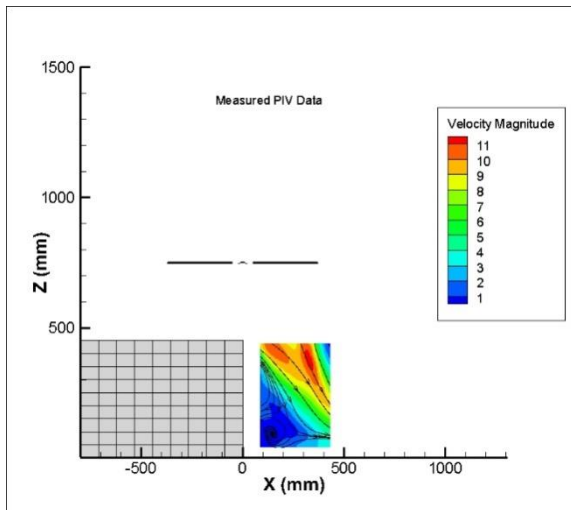


Figure 11. Measured flow pattern characteristics (averaged velocities). Rotor centre located at  $x/R = 0$ .

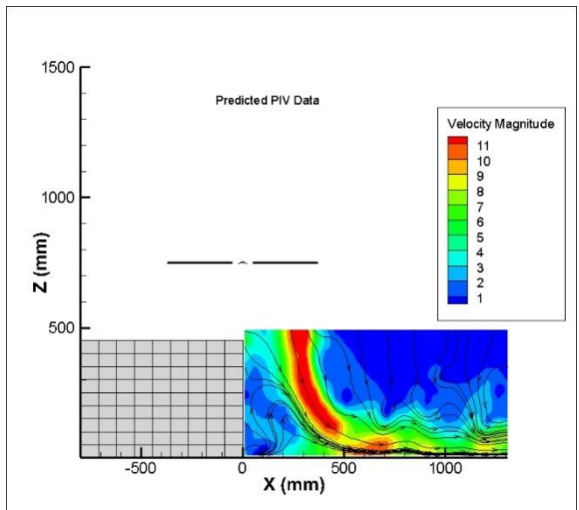


Figure 12. Predicted flow pattern characteristics (averaged velocities). Rotor centre located at  $x/R = 0$ .

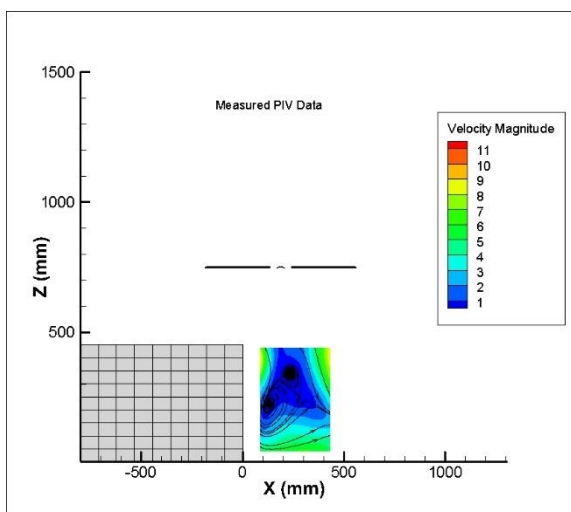


Figure 13. Measured flow pattern characteristics (averaged velocities). Rotor centre located at  $x/R = 0.5$ .

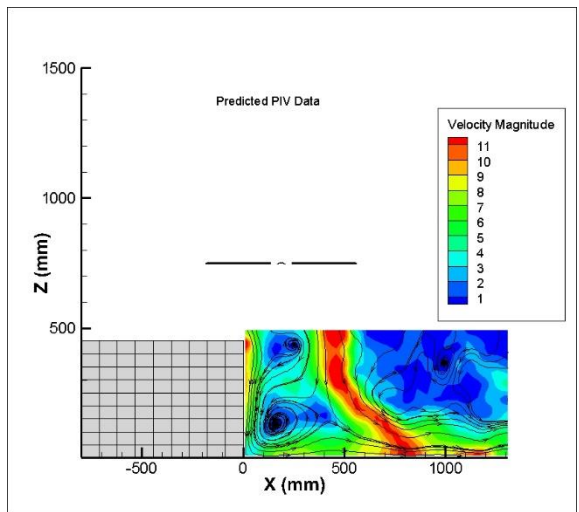


Figure 14. Predicted flow pattern characteristics (averaged velocities). Rotor centre located at  $x/R = 0.5$ .

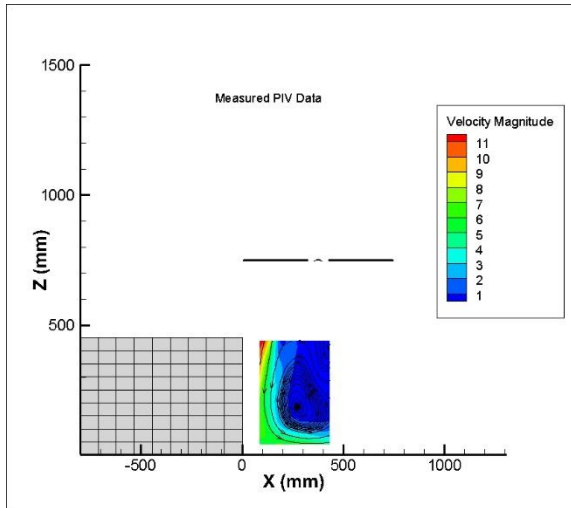


Figure 15. Measured flow pattern characteristics (averaged velocities). Rotor centre located at  $x/R = 1$ .

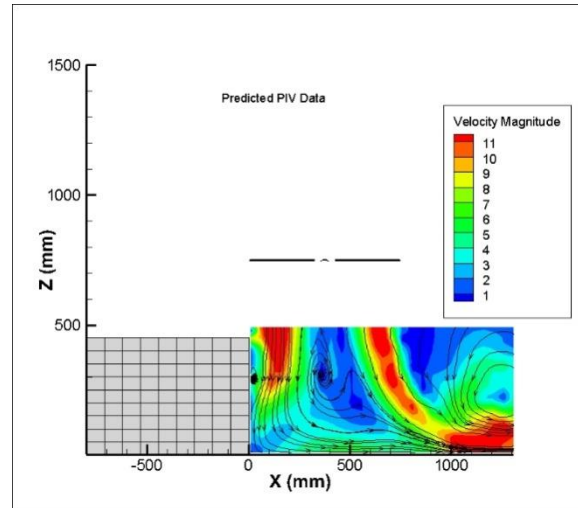


Figure 16. Predicted flow pattern characteristics (averaged velocities). Rotor centre located at  $x/R = 1$ .

Finally, when the rotor centre is at  $x/R = 1$  again no separation of the flow is noted within the measured flow pattern (Figure 15). In this case the direction of the downwash flow that impinges on the obstacle is opposite to that of  $x/R = -1$  and  $x/R = 0$ . So the wake flow moves parallel to the side face of the obstacle as in the case of  $x/R = 0.5$ . A vortex is formed beneath the centre of the rotor which in the simulations (see Figure 16) is slightly shifted upwards with respect to measurements.

### 3.2 Comparison against ONERA database

ONERA conducted a measurement campaign for a helicopter with a two bladed main rotor executing hover flight in proximity to the ground and to surrounding buildings (squared-courtyard).

#### 3.2.1 Experimental setup

The helicopter was placed at the centre of a squared-courtyard (see Figure 17 in which the coordinate system defined for the test territory is given). The diameter of the main rotor of the model helicopter was 0.71 m. The blades were composed of NACA 0012 airfoils. The nominal rotational speed of the rotor was 2600 RPM. The pitch angle of the blades was set at  $7.5^\circ$ . As concerns the dimensions of the obstacle, the height of the surrounding walls was  $h = 0.36$  m while their thickness was  $b = 0.30$  m.

Rotor thrust, velocity PIV and pressure measurements over the ground and the walls were obtained.

#### 3.2.2 Computational Setup

The computational approach is similar to that followed for the POLIMI test set-up. The only difference concerns the duration of the simulation. The side walls confine the space in which the helicopter wakes evolve. Since the distance of the

rotor from the side walls is limited, it is important to extend the simulation until the wake arrives at the walls and fills the space before any steady state results may be obtained. In this respect, a number of at least 80 revolutions were found necessary. The results presented in the sequel have been averaged over 40 periods.

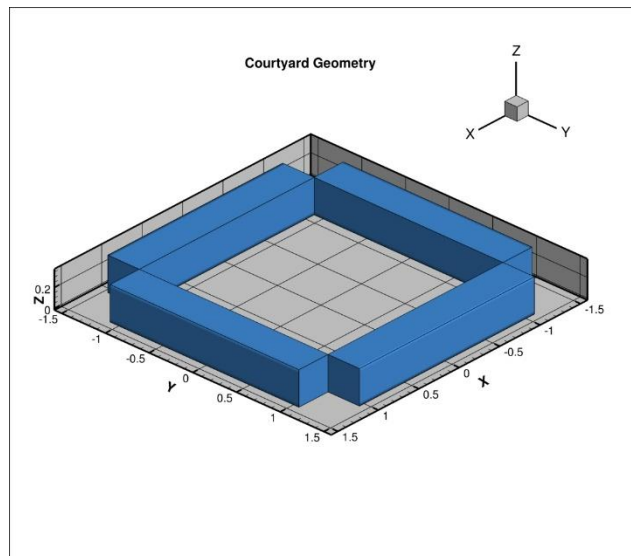


Figure 17. Global view of test courtyard.

#### 3.2.3 Rotor Loads comparison

In Figure 18 the variation of the time averaged thrust with respect to the distance from the ground is shown. The thrust ratio with (IGE) and without (OGE) ground effect is plotted versus the dimensionless distance from the ground (with respect to the surrounding walls height  $h$ ). The comparison includes results with and without the presence of the side walls. Measured data are given

in black and predictions in blue. The error bars (standard deviation) in thrust predictions indicate the range of the thrust variation that increases as the rotor distance from ground decreases. Overall good agreement between predictions and measurements is obtained. A local increase in the thrust ratio is noted in the predictions at  $z/h=1.8$  which could be an indication that more revolutions might be required in the averaging of the thrust force.

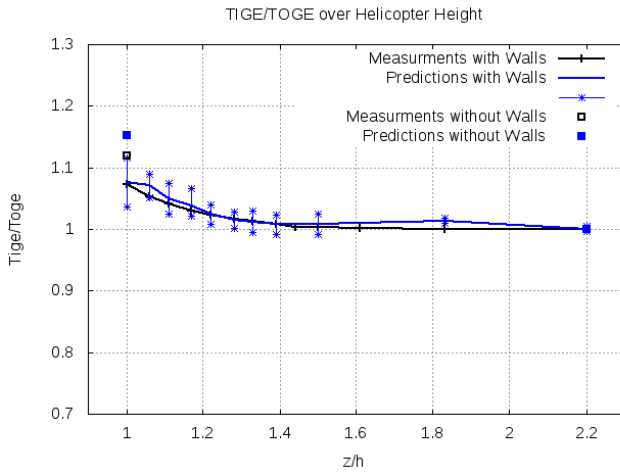


Figure 18. Thrust ratio  $T_{IGE}/T_{OGE}$  vs. dimensionless height.

The increase in thrust between  $z/h=2.2$  and  $z/h=1$  is slightly less than 10% which is lower than that obtained in the POLIMI experiment. This is attributed to the effect of the side walls. When the side walls are removed the predicted increase in thrust is 15%; exactly the same as in POLIMI set up. Measurements indicate a slightly lower increase of about 12%. So, the conclusion drawn is that in the presence of surrounding side walls, ground effect becomes less pronounced. Further explanations of the reasons behind the above described behaviour of thrust are given in the next section where flow characteristics in the interaction region are discussed.

### 3.2.4 Flow field

An effective way to explain the obtained reduction in thrust in the presence of the side walls is to analyse the developed flow field. In Figure 19 a measured pattern of the flow field (velocity PIV measurements) in the region between the rotor and the ground/walls is shown.

It can be seen that the wake of the rotor moves parallel to the ground and along the side wall before arriving at its edge. It then rolls up forming a counter-clockwise vortex which remains within the courtyard and stands in between the rotor and the walls. The vortex core lies at the same height as the rotor hub and induces downwash velocities over the rotor disc. The above flow pattern gets weaker as

the rotor moves to higher positions. In the absence of the side walls the roll up of the wake that impinges the ground would take place at a much larger distance from the rotor position and would therefore have minor effect on its performance.

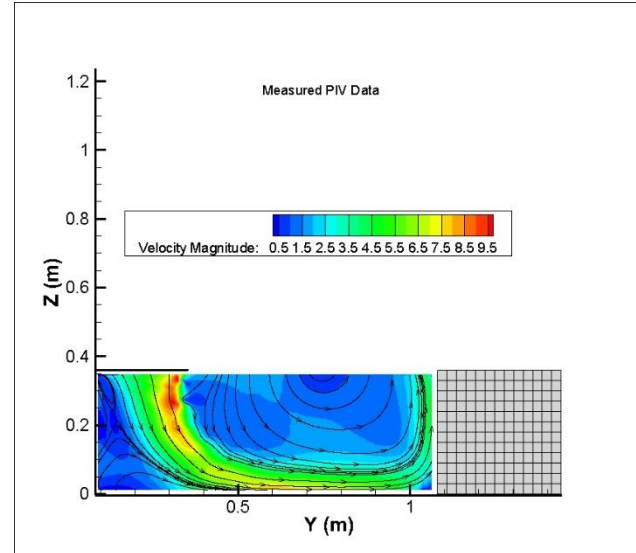


Figure 19. Measured flow pattern at  $z/h=1.01$  with surrounding walls. PIV data.

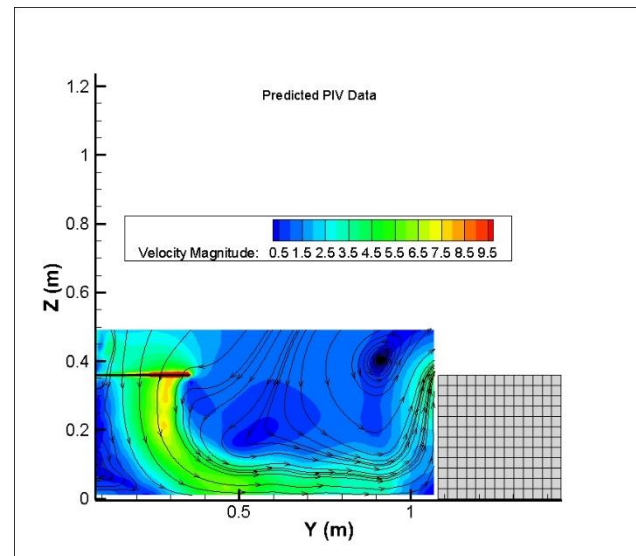


Figure 20. Predicted flow pattern at  $z/h=1.01$  with surrounding walls.

In Figure 20 a similar flow pattern is obtained through simulations. While the streamlines follow the ground and the side walls as in the tests, there is flow leakage over the side walls along their edges. Also, the rolling up of the wake is stronger and takes place closer to the walls as compared to measurements. Both of these features are attributed to the essentially inviscid character of the model which in the present case neglects the interaction with the wall boundary layer.

### 3.2.5 Ground/Wall Pressure Distributions

Next the effect of the rotor on the walls is considered as recorded in surface pressure data.

In Figure 21 the pressure distribution on the ground is shown. The helicopter performs a hover flight at  $z/h=1.01$ . Only the ground is considered and not the surrounding buildings. The test data indicate that high pressures are obtained over the area shaded by the rotor. Outside this area the pressure drops, even to negative values before it reaches its final constant mean level. Predictions show the same trend. There is also fair agreement in quantitative terms; over the area shaded by the rotor the mean level is under-predicted over its inner part ( $y < 0.25$ ) but reaches the maximum measured level when moving towards its boundary.

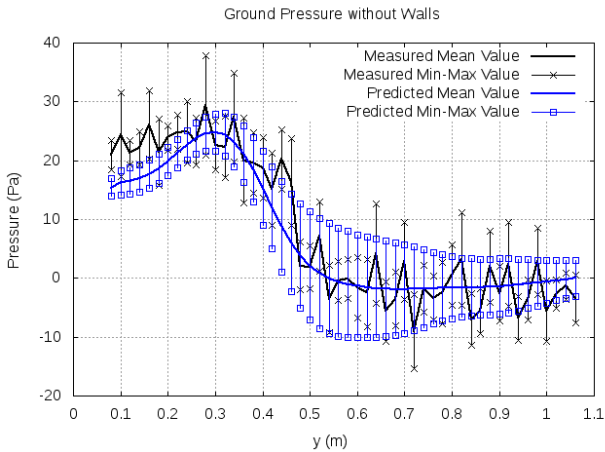


Figure 21. Ground pressure without presence of walls. Comparison of predictions against measurements.

A similar comparison is presented in Figure 22 for the case with the surrounding walls present. The main difference compared to the previous case is that the pressure drop to negative values takes place at a higher  $y$  distance. Then pressure recovers back when approaching the side walls. The predictions compare well with the test data. The level difference over the shaded area by the rotor is more uniform and the maximum level is under-predicted. This may be attributed to differences on the disk loading. Also, the negative pressure on the wall is more pronounced in the measurements. In Figure 23 comparison of the pressure distributions on the side walls is presented. Tests and predictions indicate a gradual pressure drop for increasing distance from the ground level. Overall the agreement is good. However, moving towards the edge of the side wall, there is a sudden slope increase in the predictions that is not seen in the experiments. As already noted the inviscid character of the flow solve can explain this difference which in any case remains small.

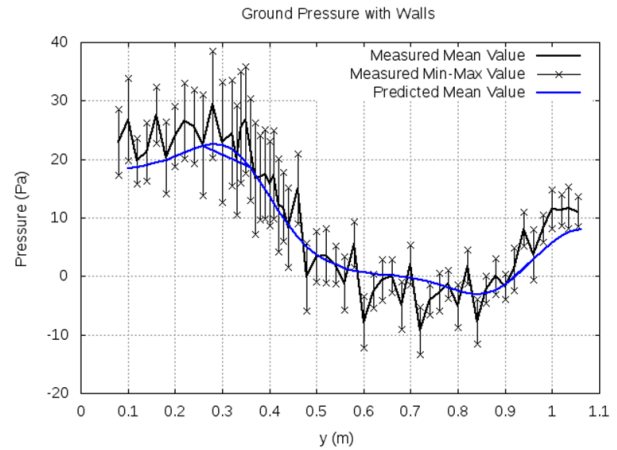


Figure 22. Ground pressure with presence of walls. Comparison of predictions against measurements.

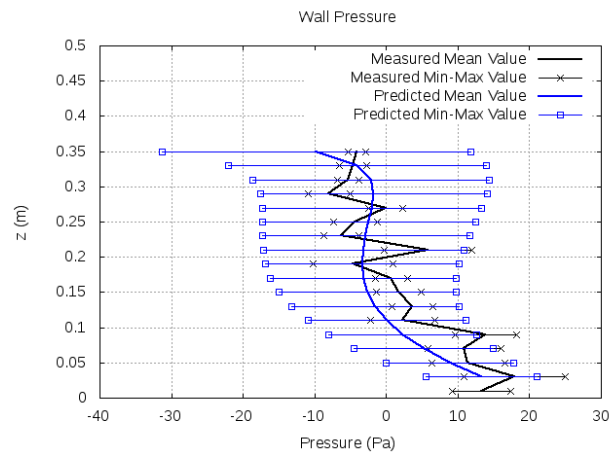


Figure 23. Wall pressures. Comparison of predictions against measurements.

### 3.3 Aeroelastic simulations

In this section aeroelastic analysis of a scaled BO105 rotor (scale factor 2.5) is performed in hover flight and in proximity to an obstacle. Assessment of the vibrations of the main rotor is performed.

#### 3.3.1 Computational setup

Hover flight simulations of a flexible BO105 rotor are performed without ground effect and in proximity to a well shaped obstacle and the ground. For the case of flight near an obstacle a configuration which is very similar to the test case T1 of the POLIMI database is selected. The helicopter rotor is centered over an obstacle of rectangular shape with dimensions 4.26 m in the  $x$ -axis, 5.36 m in the  $y$ -axis and height  $h=2.18$  m (configuration layout and coordinate system are shown in Figure 24). Hover flights at heights  $z/h=2$  and 4 have been simulated.

The simulated BO105<sup>14</sup> model consists of a four bladed main rotor which runs at 1050 RPM. The

diameter of the rotor is 4 m with  $2.5^\circ$  cone angle. Collective pitch for the undisturbed OGE case was set at  $6.92^\circ$  while trimming for constant thrust (equal to that of the undisturbed case) is performed when the rotor interacts with the obstacle and the ground.

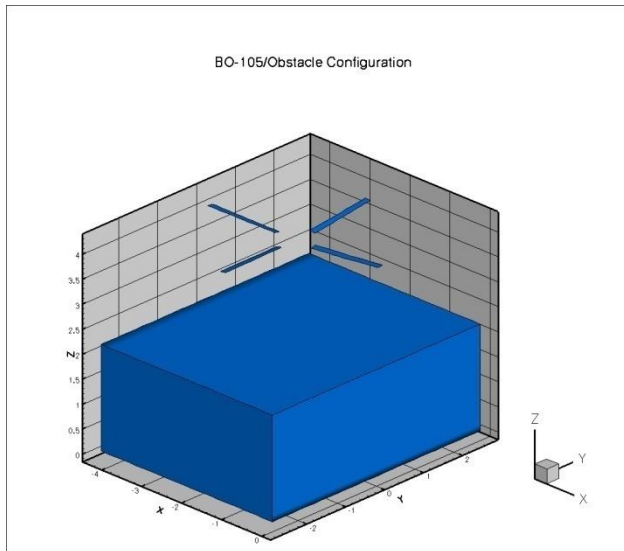


Figure 24. Global view of the simulated configuration.

### 3.3.2 Aeroelastic results

In Figure 25 the azimuthally averaged flapwise bending moment at the root of the blade is plotted for the cases of i) OGE ii)  $z/h=2$  and iii)  $z/h=4$ . Averaging of the loads has been performed over a number of 20 revolutions. It is seen that the flapwise moment of the  $z/h=2$  case exhibits a high amplitude of the 1/rev variation. It is noted that the frequency of the 1<sup>st</sup> flapwise bending mode of the BO105 rotor lies very close to 1/rev ( $\sim 17$  Hz). This indicates that interaction of the rotor with the obstacle as well as with the bouncing wake triggers low frequency

vibrations on the blades. As the height of the hover flight increases ( $z/h=4$ ) the 1/rev amplitude decreases and the azimuthal variation of the flapwise moment comes close to that of the OGE case.

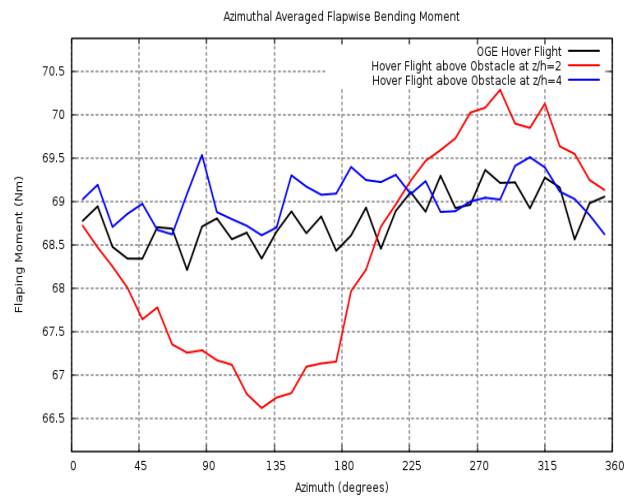


Figure 25. Azimuthally averaged flapwise bending moment at the root of the blade.

In Figure 26 the Power Spectral Density (PSD) plot of the flapwise moment is shown for the same configurations. It is seen that flight in proximity to the obstacle triggers low frequency vibrations. Not only the 1/rev peak is higher, as already seen in the azimuthally averaged results, but an additional low frequency peak ( $\sim 0.2$ /rev) rises to about the same level as the 1/rev peak. This additional peak is related to excitation by the back the bouncing wake that interacts with the rotor. The low frequency response of the  $z/h=4$  case is quite similar to the OGE case however some high frequency response (beyond 5/rev) still remains.

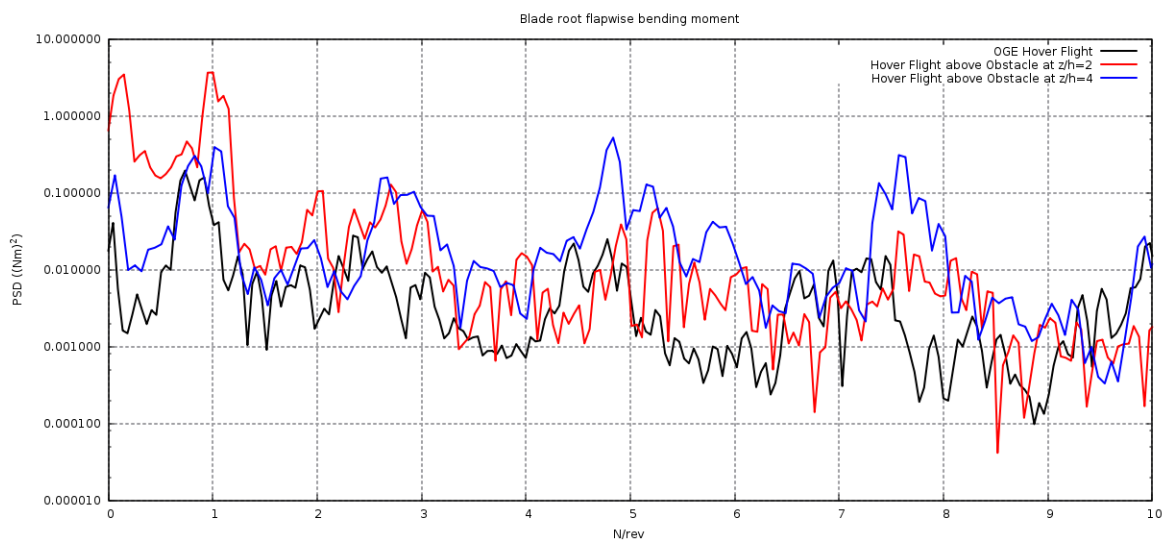


Figure 26. PSD of the flapwise bending moment at the root of the blade

#### 4 CONCLUDING REMARKS

The problem of helicopter/obstacle interaction has not yet been thoroughly numerically addressed, in particular in the context of holistic simulation environments. The present contribution addresses the topic in such a context by including all of the main interaction mechanisms in one coupled simulation. This is made possible and most importantly cost effective by using vortex methods combined with particle mesh techniques.

In the paper results of the free wake vortex particle GENUVP code with two different measurement campaigns have been compared. In the first campaign (POLIMI test campaign), interaction of a rotor with the ground and a well shaped obstacle is investigated. A thrust increase of 15% with respect to the undisturbed case is predicted when the rotor flies at 1R distance from ground which is found to be in good agreement with the measured data. Even higher thrust increase is recorded, also in good agreement with measurements when the helicopter performs hover flight in proximity to a well shaped obstacle. Lower increase in thrust (~10%) is predicted and measured in the second test campaign (ONERA test campaign) which concerns hover flight over a courtyard surrounded by walls. It has been shown that the bouncing wake rolls up within the courtyard region forming a vortex structure that induces downwash velocities over the rotor disk. In both test cases the otherwise inviscid aerodynamic model captures the rotor loads within reasonable limits however qualitative differences with respect to measurements are obtained in the simulated flow fields which are related to viscous/boundary layer effects. Nonetheless the above viscous effects do not seem to have appreciable effect on rotor loads.

Preliminary aeroelastic simulations of a BO105 model executing hover flight over an rectangular obstacle indicated that pronounced low frequency vibrations can be induced as a result of the rotor obstacle interaction.

#### 5 ACKNOWLEDGEMENTS

This work was supported by computational time granted from the Greek Research & Technology Network (GRNET) in the National HPC facility - ARIS - under project "WINDAERO" with ID pr003028.

#### 6 REFERENCES

- [1] Iboshi, N., Itoga, N., Prasad, J.V.R., Sankar, L.N., "Ground Effect of a Rotor Hovering above a Confined Area," presented at the American Helicopter Society 64th Annual Forum, Montreal, Canada, April 29-May 1, 2008
- [2] Nacakli, Y., Landman, D., "Helicopter Downwash/Frigate Airwake Interaction Flowfield PIV Surveys in a Low Speed Wind Tunnel," presented at the AHS International 67th Annual Forum & Technology Display, Virginia Beach, VA, USA, May 3-5, 2011
- [3] Visingardi, A., "Forces on Obstacles in Rotor Wake - Terms of Reference for the GARTEUR Action Group HC/AG-22 – Vsn. 1," November 2014
- [4] Voutsinas, S. G. (2006). Vortex methods in aeronautics: how to make things work. *International Journal of Computational Fluid Dynamics*, 20(1), 3-18.
- [5] Papadakis, G., &Voutsinas, S. G. (2014). In view of accelerating CFD simulations through coupling with vortex particle approximations. In *Journal of Physics: Conference Series* (Vol. 524, No. 1, p. 012126). IOP Publishing.
- [6] Manolas, D. I., Riziotis, V. A., &Voutsinas, S. G. (2015). Assessing the importance of geometric nonlinear effects in the prediction of wind turbine blade loads. *Journal of Computational and Nonlinear Dynamics*, 10(4), 041008.
- [7] Gibertini, G., Zagaglia, D., "Existing databases identified: Polimi Experimental Database in absence of wind," Doc. GARTEUR\_HC-AG22-WP1-TR-01, January 2016
- [8] J.L. Hess, "Calculation of potential flow about arbitrary three-dimensional lifting bodies", McDonnell Douglas Rep., MDC J5679-01, 1972.
- [9] C. Rehbach, "Calcul d'écoulements autour d'ailes sans épaisseur avec nappes tourbillonnaires évolutives », *Recherche Aérospatiale* 2:53-61, 1973.
- [10] G-H Cottet, P.D. Koumoutsakos, "Vortex methods: Theory and Practice", Cambridge University Press, 2000
- [11] S.M. Richardson and A.R.H. Cornish, "Solution of three dimensional incompressible flow problems", *J. Fluid Mechanics*, Vol 82, 309-319, 1977

- [12] J.T. Beale and A. Majda, "Higher order accurate vortex methods with explicit velocity kernels", J. Comput. Physics, Vol 58, 1985
- [13] Paquet, J.B., Bourez, J.P., "Torseur de efforts aerodynamique sur un rotor a pas fixe: effet de sol et visualisations" Rapport technique ONERA No 1/22265 DAAP (Avril 2015)
- [14] Dieterich, O., Langer, H.J., Sneider, O., Imbert, G., Hounjet, M.H.L., Riziotis, V., Cafarelli, I., Calvo Alonso, R., Clerc, C., Pengel, K. (2005) "HELINOVI: Current vibration Research activities", 31st European Rotorcraft forum, Florence, Italy, September 13-15, 2005.